# Terahertz ultrasensitive biosensor based on wide-area and intense light-matter interaction supported by QBIC

Bingwei Liu [a], Yan Peng [a,*], Zuanming Jin [a], Xu Wu [a], Hongyu Gu [a], Dongshan Wei [b,*], Yiming Zhu [a,*], Songlin Zhuang [a]

[a] *Terahertz Technology Innovation Research Institute, Terahertz Spectrum and Imaging Technology Cooperative Innovation Center, Shanghai Key Lab of Modern Optical System, University of Shanghai for Science and Technology, Shanghai 200093, China*
[b] *School of Electrical Engineering and Intelligentization, Dongguan University of Technology, Dongguan 523808, China*

ARTICLE INFO

ABSTRACT

A quasi-bound state in the continuum (QBIC) has unique attraction in optical switch, nonlinearity, communication, and sensing due to its ultrahigh radiation quality (Q) factor. The QBIC observed in metasurfaces also provides a feasible platform to achieve in-plane strong light-matter interaction, as well as to develop ultrasensitive biosensor. However, the existing metasurface designs are difficult to realize highly efficient excitation and high-performance sensing of QBIC in terahertz (THz) band. Here, we manipulate the interference coupling between electric quadrupole and magnetic dipole by introducing an asymmetry $\alpha$ into the metallic metasurface structure, which excites ultrahigh quality QBIC resonance with Q factor of up to 503. Correspondingly, light field energy constrained by the metasurface and effective sensing area achieved enormous increases of about 400% and 1300%, respectively, which greatly expands the spatial extent and intensity of light-matter interaction. Simulations and experiments show that the proposed QBIC metasurface deliver a high refractive index sensitivity reaching 420 GHz/RIU, where RIU is the refractive index unit, and its direct limit of detection (LoD) for trace homocysteine (Hcy) molecules is 12.5 pmol/μL. Its performance is about 40-times better than that of the classical Dipole mode. This work provides a new avenue to achieve rapid, precise, and nondestructive sensing of trace molecules, and has potential applications in the fields of biochemical reaction monitoring, photocatalysis and photobiomodulation.

## 1. Introduction

The metasurface is an ultrathin, patterned artificial surface consisting of optical subwavelength resonantors, so called meta-atoms, arranged in a periodic fashion [1–5], which has been widely applied as an ideal platform for studying and tailoring light, and has made a number of breakthrough achievements in hologram or computational imaging [6,7], communication [8], near-field microscopy [9], and sensors [10–12]. By combining or tailoring meta-atoms, various optical resonance phenomena can be manipulated and induced, such as surface plasmon resonance (SPR) [13], super-lattice resonance [14–16], electromagnetic induced transparency (EIT) [17,18], Fano resonance [19–21], Mie resonance [22,23], etc. These can be used to explore technological innovations and applications in the frontiers of optics and even physics research, including laser nonlinear effect [24], biochemical molecule sensing [25], light storage and operation [26,27], and smart labeling [28]. Recently, THz technology has attracted great interest in the field of chemistry and biomedicine due to its unique advantages such as strong penetration, nonionizing, and non-destructive [29–31]. The rotation and vibration of a large number of biomolecules also provide spectral fingerprints in terahertz band for identification [32–35]. The combination of metasurfaces and terahertz sensing technology owns the advantages of both label-free and high sensitivity, and it can enhance the coupling between analyte and the electromagnetic wave [36]. The design flexibility of metasurfaces also supports customized sensing of various samples [37,38]. Although several terahertz biosensing methods based on metasurfaces have been reported, which can identify analytes with specific refractive index according to the resonance shift, such as cells [39], proteins [40], viruses [41], etc. However, previous metallic or dielectric metasurfaces biosensors generally have low sensitivity. Because their resonant modes naturally have a low Q factor [42,43], and are further attenuated by the influence of ohm or radiation loss, which

makes the detection capability of biosensors into a bottleneck. In addition, many biological samples obtained in clinical practice are usually trace (≤nmol level), and some disease biomarker molecules even cannot rely on the nanoparticle-antibody system to amplify signals [44,45], which further increases the difficulty of identifying such samples by low-Q metasurface biosensors.

Fortunately, the concept of bound state in the continuum (BIC) has been introduced into the design of metasurfaces in recent years [46–48]. In photonic systems, BIC behaves as a special mode characterized by energy being bound in a continuum, and unable to couple with free space radiation. Theoretically, it delivers ultrahigh or even infinite radiation Q factor and infinite lifetime [49,50], which has the non-radiative property of spectral linewidth disappearance. But the introduction of external perturbations can make BIC produce limited leakage and become an observable quasi-bound state in the continuum (QBIC) [51–53]. The properties of QBIC include extremely narrow linewidths observed in the far field, and the ability to capture more electromagnetic energy for longer time in the resonant cavities, which can achieve strong enhancement of the local light field, and led to its numerous optics applications [54–57]. Currently, potential applications of optical metasurface biosensors based on BIC in the field of biochemical sensing have begun to be explored, including fingerprint spectrum acquisition, molecular recognition, circular dichroism (CD) enhancement, flexible metasurfaces, and microfluidic refractive index sensing [58–65]. However, these works mainly focus on theoretical studies, and all predict that there may be a huge Q factor attenuation of the fabricated metasurfaces. This is caused by the inevitable Ohmic loss or radiation loss, as well as limitations of existing instrument accuracy,

and especially the latter suppresses the robustness of QBIC [66]. In addition, the explanations of QBIC sensing mechanism in existing research are not in-depth and, more importantly, lack experimental verification. Therefore, theoretically and experimentally, exploring the optical sensing mechanism of QBIC, especially studying its constraint law on electromagnetic field energy and realizing the controllable amplification of the strong light-matter interaction, will be helpful to solve the challenges in the development of high-Q metasurface biosensors.

In this work, we proposed a 'ring chain' metasurface based on QBIC. Under the excitation of THz pulse, the introduction of structural asymmetry will lead to interference coupling between electric quadrupole and magnetic dipole, and the QBIC resonance can be observed in the far field, which has ultrahigh or even infinite Q factor. Based on theoretical simulation, we found that QBIC has better sensing performance than eigen Dipole resonance. This is due to the following two points: 1) the huge increase in the effective sensing area realized by the spatial coupling of electromagnetic fields; 2) the strong light field constraints determined by high Q factor, which greatly expand the spatial extent and intensity of in-plane light-matter interaction. We can also control the Q factor and resonance intensity of QBIC by optimizing the asymmetry, which depends on different biological samples and system resolution. Here, our proposed QBIC metasurface exhibits ultrahigh Q factor of up to 503, and the theoretical sensitivity is up to 420 GHz/RIU. It can realize high performance sensing near 2 THz, and the direct limit of detection (LoD) for biomarker homocysteine (Hcy) can reach the pmol level. Our results show that this QBIC metasurface biosensor can serve as a strong and powerful tool for high performance sensing of trace
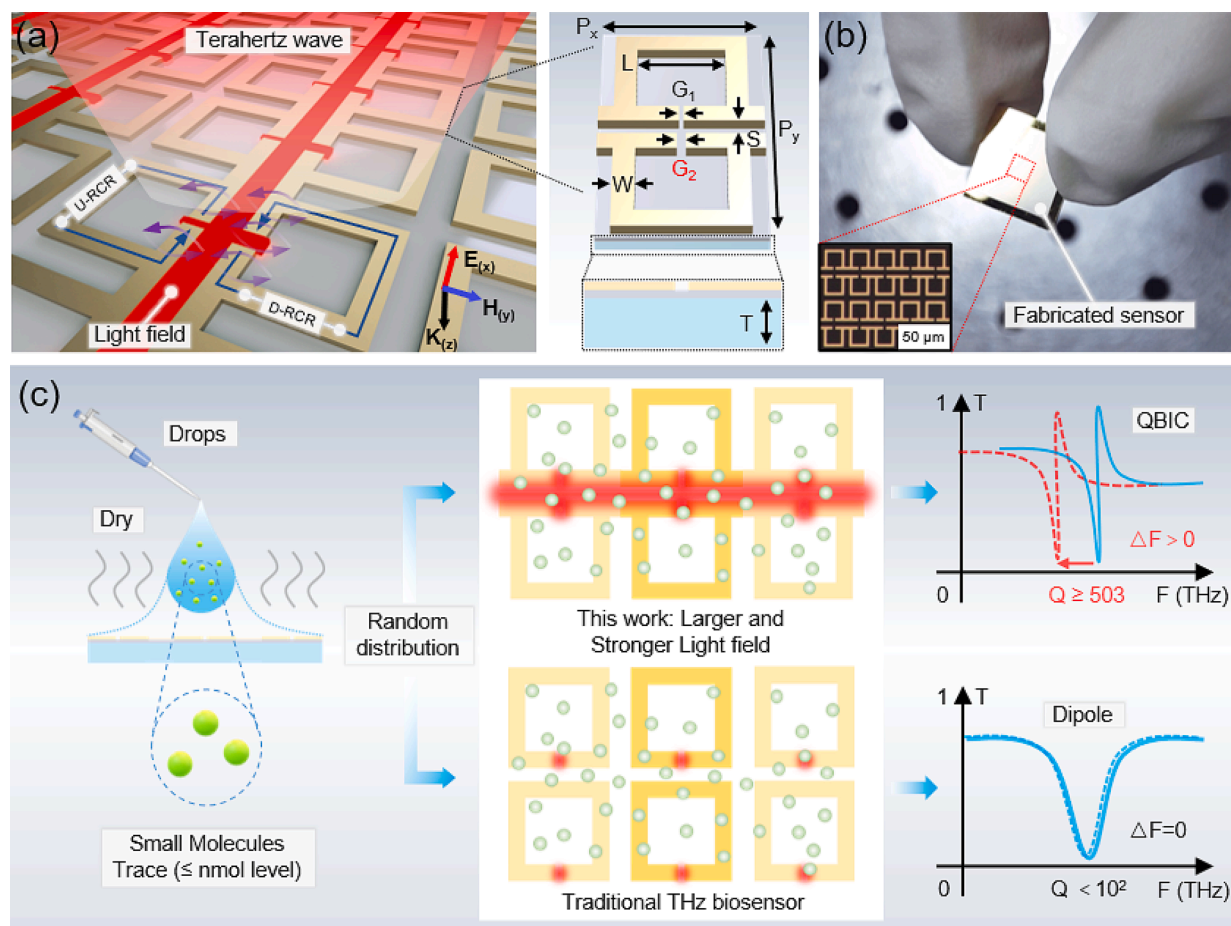


**Fig. 1.** The design concept of our proposed QBIC metasurface biosensor. (a) The schematic diagram of QBIC metasurface excited by THz wave and the geometric parameters of the lattice. (b) The fabricated metasurface biosensor and micrograph of bare metasurface structures. (Scale bar = 50 μm). (c) The sensing advantages of the proposed metasurface for trace molecules are introduced.

biomolecules, and can be generalized to cross wavelength regions beyond the THz band.

## 2. Material and methods

### 2.1. Design strategy of the metasurface biosensor

Fig. 1a shows the schematic diagram of our proposed metallic QBIC metasurface biosensor. It consists of a periodic array of two ring chain resonators with different gap widths machined on a rectangular lattice. For the convenience of distinction, we define these two resonators as up ring chain resonator (U-RCR) and down ring chain resonator (D-RCR). Under the excitation of THz pulse, there is a pair of reverse current oscillations in the loops of resonators (blue arrows), and each generates a circular magnetic field (purple arrow). They are coupled at resonator cavities and the large gap region between resonators, thus showing a wide-area and super-strong binding behavior to the incident light field (Fig. 1a, left). The resonator and substrate materials are gold and quartz, respectively. For the geometric parameters of the lattice, the periods along the x- and y-directions are $P_x = 37$ μm and $P_y = 74$ μm, and thickness of substrate is $T = 500$ μm. In the x-y plane, $L = 30$ μm, $W = 5$ μm, $S = 7$ μm, $G_1 = 2$ μm, $G_2 = 3$ μm. It should be noted that the gap width $G_2$ of D-RCR is variable to introduce asymmetry and the other parameters remain unchanged (Fig. 1a, right). For studying electromagnetic characteristics of the excited QBIC resonance, we define gap width difference $\Delta G = G_2\text{-}G_1$ and the asymmetry $\alpha = \Delta G/G_1$. The proposed metasurface first deposits chromium and gold films on a double-sided polished quartz substrate, and then uses conventional lithography technology for patterning. It should be noted that chromium is used as a bonding layer. The schematic diagram of the fabricated biosensor is shown in Fig. 1b, and the structure is locally magnified for observing.

In order to demonstrate the sensing advantages of the proposed metasurface biosensor for trace molecules, we described its details in Fig. 1c. In the THz sensing method based on metasurfaces, the reagent containing the sample molecules contacts the biosensor surface by dropping samples. After drying, the sample molecules will be freely distributed and attached to the biosensor surface in the form of films or small clusters. For many small biomarker molecules, including Hcy, the clinically obtained samples are usually trace (nmol or even pmol level) and have the characteristics of random distribution on the biosensor surface (Fig. 1c, left). In addition, unlike many viruses or nucleic acids, some biomarker molecules are even difficult to amplify signals by means of nanoparticle hybridization. Therefore, the detection results are highly dependent on the Q factor of the biosensor and the size of the effective sensing area. For the traditional THz metasurface biosensors, the light field is confined in their resonant cavities with small area, the probability of the sample molecules falling inside the resonant cavities is low. And their resonance modes usually have a lower Q factor, thus losing the ability to identify trace samples. However, for our proposed QBIC metasurface biosensor, it has a wide-area and ultra-strong photoactive region to 'capture' more sample molecules, and its sharp resonance peak is enough to distinguish trace level samples (Fig. 1c, middle & right).

### 2.2. Numerical simulations

In order to study the potential resonance mechanism and spectral responses of our proposed QBIC metasurface, numerical calculations were carried out using Comsol Multiphysics (version 5.4). Floquet periodic conditions were set in free space along the x- and y-directions, a perfect match layer (PML) was taken in the z-direction as the absorption boundary. The excitation field was an x- or y-polarization plane wave propagating along the z-direction. Convergence results were obtained by setting the grid smaller than the critical structure minimum size. The dielectric constant of the quartz substrate was 3.9. The resonator material can be set as a perfect conductive (PEC) to simplify the operation.

### 2.3. Sample preparation and testing

In order to demonstrate the trace molecular sensing performance of QBIC metasurface biosensor, we selected the low concentration Hcy aqueous solution as the test object. The pure Hcy used here is provided by Sigma-Aldrich and the solvent is ultrapure water. It should be noted that our previous work has proved the stability of Hcy in aqueous solution [45]. In the experiment, we uniformly configured 6 groups of Hcy samples with different concentrations (the corresponding concentrations were 0.0125, 0.05, 0.5, 2.5, 10 and 40 nmol/uL, respectively). The amount of each group of samples dropped on the biosensor is 20 μL (the corresponding Hcy contents were 0.25, 1, 10, 50, 200, 800 nmol, respectively). We promoted random and uniform distribution of molecules through rapid drying treatment. The sample testing was carried out with a commercial terahertz spectrometer (Advantest TAS7400). The effective spectral range is from 0.5 to 4 THz, and the spectral resolution is about 7.6 GHz. In order to suppress the interference of water vapor, all our tests were carried out at room temperature of 23 °C and relative humidity of less than 3 %. All samples are tested repeatedly to ensure the robustness of the results, and Fourier transform was used to obtain the frequency domain signals (see Supplementary Material S1 for details).

## 3. Results and discussion

### 3.1. QBIC characteristics and metasurface performance optimization

In order to analysis the formation mechanism of the excited QBIC, we calculated the transmission spectra under x- and y-polarized THz waves with the D-RCR gap width $G_2$ varying from 0.5 to 10 μm ($\alpha = 0.25 \sim 4$). As shown in the top panels of Fig. 2a & b, QBIC resonances can be excited under both x- and y-polarized THz waves, and the BIC positions are consistently located at 2.025 THz. When $\alpha = 0$, the resonances at the BIC position in the transmission spectra disappear simultaneously, at which point the structure is in the symmetry-protected BIC state with infinite Q factor and the energy is bound here without leaking into the free space. With the increase of $\alpha$, the linewidth of resonance gradually decreases, and blue shift occurs. This is because when $\alpha \neq 0$, the structural symmetry is broken, and the symmetry-protected BIC state begin to transform into QBIC with finite leakage rate. In the bottom panel of Fig. 2a, the blue shift evolution of two resonance modes (Dipole mode and QBIC mode) is observed under x-polarized THz waves. It is obvious that the introduction of asymmetric perturbation breaks symmetry-protected BIC state and evolves to QBIC resonance with extremely narrow linewidth on both sides, after which followed a trend from narrow to wide. While in the bottom panel of Fig. 2b, under y-polarized THz waves, only the evolution of QBIC mode can be observed. Although the QBIC resonance linewidth at this position seems to be very narrow, its resonance amplitude and linewidth are mutually constrained, resulting in poor resonance intensity and difficult to observe, which is very unfavorable for experimental sensing. In addition, we investigated the relationship between the resonance Q factor and the asymmetry $\alpha$. And fitted the transmission spectra with a typical Fano lineshape formula $T_{Fano} = \left| a_1 + ja_2 + \frac{b}{\omega - \omega_0 + j\gamma} \right|$ to extract the Q factors [49], where $a_1$、$a_2$ and $b$ are real constant factors, $\omega_0$ and $\gamma$ are the resonance frequency and damping rate, respectively, and the Q factor can be calculated by $Q = \omega_0/(2\gamma)$. Note that all unknown parameters are specified in the interval [0,1]. In Fig. 2c & d, the divergence trajectory of the Q factor is mapped by different $\alpha$. When $\alpha$ tends to 0, the Q factor of QBIC supported by x- and y-polarized terahertz waves is close to infinity. And for two structures with equivalent $|\alpha|$ values, they all have almost the same Q factor, and the dependence of Q factor on $\alpha$ also follows the inverse-quadratic $\alpha^{-2}$. Research shows the BICs excited in metasurfaces are mainly divided into symmetry-protected BIC and accidental BIC [67–70], the former exists at the center of the Brillouin zone and is
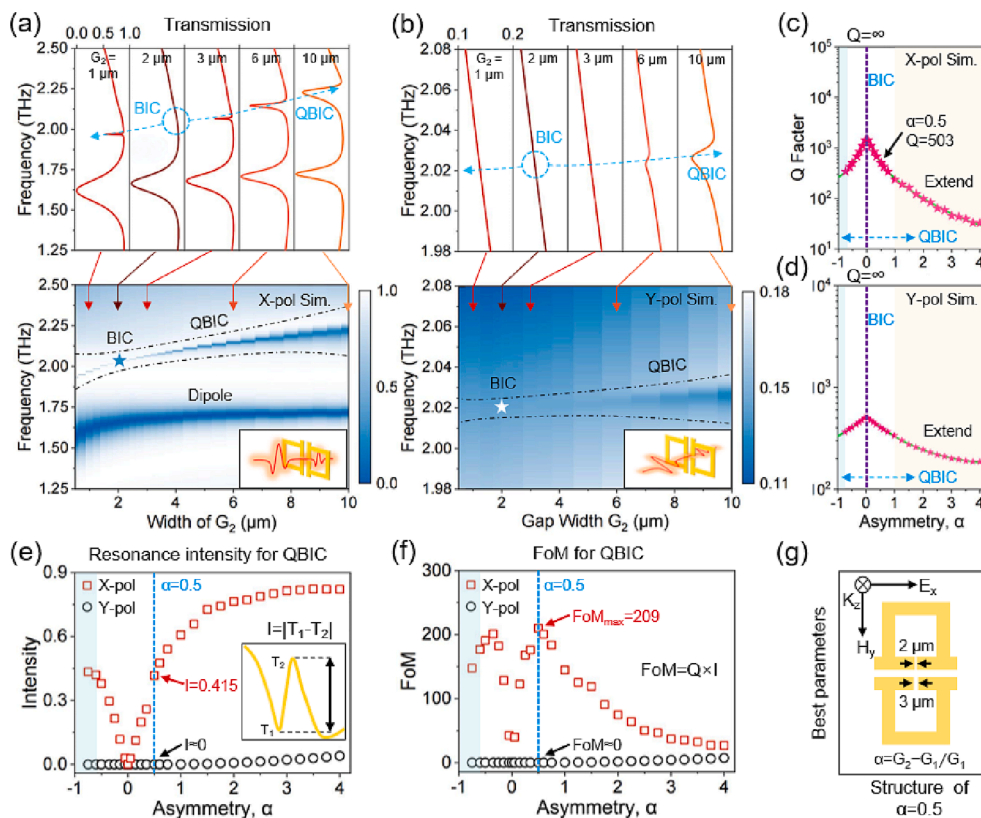
**Fig. 2.** The evolution characteristics of QBIC and the performance optimization of our proposed metasurface under x- and y-polarized THz waves. (a,b) Simulated the transmission spectra of the structure with different gap widths $G_2$. Bottom: Adjusted $G_2$ from 0.5 to 10 μm. The BIC position (star) appears at $G_2 = 2$ μm, where is under symmetry-protected state and has no leakage. Top: Spectral tracking of QBIC evolution in five representative asymmetric states. The BIC is marked with a virtual coil and the arrow tracks the evolution of the transmission sag. The insets show that the metasurface is excited by x- or y-polarized THz waves. (c,d) Extracted Q factors of QBIC modes corresponding to different asymmetry α. Vertical coordinates show the Q factors on the log scale as a function of α. Stars are calculated data points. The left blue shaded region cannot be observed in the experiment. The middle blank region contains the symmetry-protected BIC state. The right yellow shaded area is used to observe the evolution of Q factors. The nonlinear fit to the data points was performed, all with $R^2 > 0.99$. (e,f) Calculated resonance intensity and general figure of merit (FoM) of QBIC modes corresponding to different asymmetry α, where I=| $T_1$-$T_2$| and FoM = Q × I. (g) Ideal metasurface parameters corresponding to FoM$_{max}$ = 209 (α = 0.5), where $G_1$ = 2 μm, $G_2$ = 3 μm. (For interpretation of the references to colour in this figure legend, the reader is referred to the web version of this article.)

excited by an in-plane symmetry mismatch, while the latter is usually excited an isolated band of the accidental in-plane wave vector. Interestingly, they all obey the inverse-square law $Q = Q_0|\alpha|^{-2}$ formulated by Koshelev et al., which reflects the increase in the asymmetry of the system (α) leading to the Q factor attenuation of the resonance, where $Q_0$ is a constant independent of |α| and is determined by the metasurface itself [71,72]. These evidences indicate that the QBIC resonance studied in this work is excited by symmetry-protected BIC.

Next, we optimized the metasurface performance parameters based on the evolution of QBIC. In Fig. 2e, the evolution trend of QBIC resonance intensity under x-polarized incidence is opposite to that of the Q factor, because there exists mutual constraint between the resonance intensity and the linewidth. In addition, the corresponding resonance intensity under y-polarized incidence is generally weak. The parameter I=|$T_1$-$T_2$| is to describe the transmission intensity of QBIC resonance, where $T_1$ corresponds to the peak value of the asymmetric lineshape and $T_2$ corresponds to the inclination position, as shown in the inset of Fig. 2e. Furthermore, a general figure of merit (FoM) [62] is introduced to obtain the best tradeoff between Q factor and resonance intensity, and here FoM = Q × I. So as to evaluate the optimal performance of the metasurface at different α. In Fig. 2f, under x-polarized incidence, the QBIC resonance excited by the metasurface at α = 0.5 corresponds to FoM$_{max}$ = 209 and has an ultrahigh Q factor of 503, which is an ideal parameter for optimizing metasurface performance. In addition, the structure of this parameter also excites an eigen Dipole resonance of Q = 15 at low frequency position. It can be found that the Q factor of the excited QBIC resonance is at least one order of magnitude higher than that of the eigen Dipole resonance, which is an extremely surprising result. It is worth noting that linewidth of Dipole resonance becomes consistently narrowed as α increases until it tends to stabilize (Fig. 2a, bottom panel), which implies that the introduction of asymmetric perturbation also improves the quality of Dipole resonance (see

Supplementary Material S2 for details). In Fig. 2g, the optimal metasurface structure parameters and polarization conditions corresponding to FoM$_{max}$ (α = 0.5) are also drawn for viewing. Since the position and performance of QBIC resonance can be easily controlled by the asymmetry α, we can flexibly customize the corresponding optical manipulation and sensing platform for different optical application scenarios and actual detection conditions.

### 3.2. Wide-area and intense light-matter interaction supported by QBIC

Different from the classical Dipole mode, QBIC has unique electromagnetic field manipulation law and optical sensing mechanism. Based on the proposed metasurface, we have explored this in depth and demonstrated the wide-area and intense light-matter interaction supported by QBIC, which will lead to QBIC resonance having stronger sensing performance than that of Dipole resonance. The metasurface at α = 0.5 under x-polarized incidence is discussed here because it is an optimized ideal structure. Firstly, we study the influence of electromagnetic field coupling between U-RCR and D-RCR on the sensing, and the corresponding α is 0 and 0.5, respectively. For Dipole resonance, the electric field enhancement in the x-y plane is mainly distributed in the inner part of resonant cavities and its side edge, and the formed annular electric field flows in the same direction clockwise. There is no obvious coupling between U-RCR and D-RCR at this time (Fig. 3a, left), and the simulation results of single resonator and double resonator arrays further prove this deduction (see Supplementary Material S3 for details). Accordingly, the magnetic field enhancement in the y-z plane of Dipole resonance is mainly limited to the near surface of resonators. The annular magnetic fields at two resonators are distributed in the same direction along the Z axis, and there is no obvious coupling between them. The spatial distribution volume of magnetic field is small and the magnetic field intensity is weak (Fig. 3c, left). But for QBIC resonance,
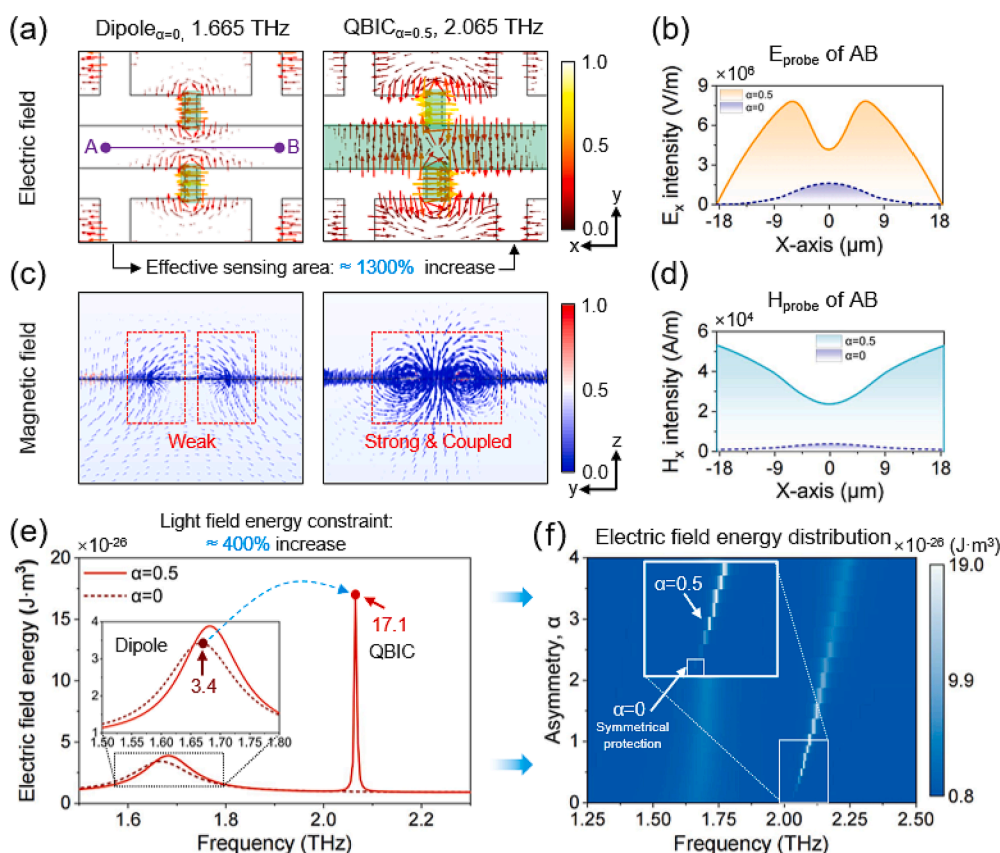
**Fig. 3.** The manipulation of the light field by Dipole mode and QBIC mode under x-polarized incidence. (a) The displacement electric field density distribution in x-y plane corresponding to Dipole resonance (1.665 THz) and QBIC resonance (2.065 THz). Green masks represent the effective sensing areas. Red frames represent the magnetic field interaction regions. (b) Extracted the electric field intensity distribution corresponding to probe AB in x-y plane when $\alpha = 0$ and $\alpha = 0.5$. (c) The spatial magnetic field density distribution in y-z plane corresponding to Dipole resonance (1.665 THz) and QBIC resonance (2.065 THz). (d) Extracted the magnetic field intensity distribution corresponding to probe AB in x-y plane when $\alpha = 0$ and $\alpha = 0.5$. (e) Compared the constrained electric field and magnetic field energy between Dipole resonance and QBIC resonance. (f) Simulated the frequency domain distributions of electric field energy constrained by metasurfaces at different $\alpha$. The position of $\alpha = 0$ and $\alpha = 0.5$ is marked by white arrows. When $a = 0$, it is in asymmetry-protected state. (For interpretation of the references to colour in this figure legend, the reader is referred to the web version of this article.)

the electric field enhancement in the x-y plane is not only distributed in the inner part of resonant cavities and its side edges, but also exists in the large gap region between U-RCR and D-RCR. We speculate that this position forms a large 'photoactive region' (Fig. 3a, right). And the magnetic field distribution in the y-z plane indicates that there are two extremely strong annular magnetic fields at the resonant cavities. They are distributed counterclockwise and clockwise along the z-direction respectively, and start to decay when they are far away from the resonator. Interestingly, these two magnetic fields are closely superimposed in the intersecting region and coincide with the presumed 'photoactive region'. This strong coupling means that the interaction between electromagnetic field and matter will be much stronger than that of Dipole resonance (Fig. 3c, right). It can also be found that the magnetic field region of QBIC resonance shows a larger extension range than that of Dipole resonance from the z-direction, which is more conducive to the full interaction between light field and analytes. In Fig. 3b & d, we set the probe AB in the x-y plane to extract the electric field and magnetic field intensity distribution in the large gap region between U-RCR and D-RCR of two modes. It can be found that the corresponding electric and magnetic field intensities of QBIC mode have super-strong distribution characteristics in the spatial domain, and have complementary overall responses. Therefore, the presence of this large range photoactive region induced by QBIC can be confirmed, which greatly expands the spatial extent of the in-plane light-matter interaction and means a huge increase in the effective sensing area. The calculated total sensing area of QBIC resonance is increased by about 1300% compared with eigen Dipole resonance (the area marked by the green mask in Fig. 3a is the effective sensing area).

Next, we compare the ability to constrain the electric field energy of Dipole resonance and QBIC resonance excited by metasurface at $\alpha = 0$ and 0.5. In Fig. 3e, the electric field energy constrained by QBIC resonance is much stronger than that of Dipole resonance, and the distribution is very concentrated, which increases by about 400 % (the

inset gives the enlarged version of Dipole resonance position). This result means that the light field at the QBIC resonance position stores more electromagnetic energy for coupling with the analyte, which will greatly expand the intensity of the in-plane light-matter interaction and can detect more ultrathin samples. In Fig. 3f, we calculated the total frequency domain distribution of electric field energy constrained by the metasurfaces at different $\alpha$. Interestingly, its distribution law is consistent with the bottom panel of Fig. 2a. When $\alpha = 0$, there is no electric field energy leakage, which corresponds to the symmetry-protected BIC state. When $\alpha \neq 0$, a large increase in electromagnetic energy can be observed at nearby QBIC position. With the increase of $\alpha$, the electromagnetic energy attenuates, which is caused by the increase of the leakage rate. This degeneration phenomenon can also be confirmed by the inverse-quadratic law $\alpha^{-2}$ obeyed by the Q factor in Fig. 2c. In addition, for Diploe resonance, the constrained electromagnetic energy always increases with the increase of $\alpha$, and tends to be stable near $\alpha = 4$ (see Supplementary Material S4 for details).

The qualitative and quantitative evidences in the above analysis show that wide-area and intense light-matter interaction supported by QBIC makes the proposed metasurface become an ideal platform for manipulating light and realizing highly sensitive biochemical molecular sensing. Since the analyte is usually randomly distributed on the metasurface, the larger effective sensing area means that the greater probability of analyte falling into it. Furthermore, considering that in the practical sensing, even if the interference of human factors is ignored, the probability of the molecule to be measured at nmol level falling into the effective sensing area will only be lower [41], which is extremely unfavorable for the detection of trace molecules (such as pmol level). Therefore, this QBIC metasurface not only increases the probability that the molecule to be measured falls into the effective sensing area, but also promotes the interaction between electromagnetic energy and matter due to its super-strong optical field constraint. This will greatly enhance the sensitivity of the metasurface biosensor and produce more

significant resonance frequency shift for fewer samples. As far as we know, a few reported references claim that QBIC resonance has stronger sensing performance [61–63], but they usually attribute it to the higher Q factor of QBIC resonance according to the simulation results, and lack of relevant experimental verification. Therefore, our detailed analysis and interpretation of the light field manipulation and sensing mechanism of QBIC in this work are still the first time in the existing research, which fills the gap in the previous research.

### 3.3. Multipolar decomposition and resonance mode analysis

We take the metasurface structure of $\alpha = 0.5$ as the research object to quantitatively analyze the dominant components of QBIC resonance. Here, the THz electric field is polarized along the x-direction (Fig. 4a, inset). we performed the Cartesian multipolar decomposition for the far-field scattering power of the metasurface, which mainly includes electric dipole (ED), magnetic dipole (MD), electric quadrupole (EQ), magnetic quadrupole (MQ) and ring dipole (TD) (see Supplementary Material S5 for details). Here, we ignored the high-order components of multipole expansion in calculation because their contributions are very small. In Fig. 4a, the symmetry-protected BIC state in the continuous spectrum is broken at 2.065 THz, and an observable very narrow QBIC resonance is formed. This QBIC mode is mainly controlled by EQ, and the contribution of MQ cannot be ignored. These two components interfere with each other and other multipolar components are strongly inhibited. The mode distribution of QBIC resonance is also plotted (Fig. 4b, right). Under the perturbation of asymmetry, both U-RCR and D-RCR excite the reverse current distribution, and jointly form the strong EQ mode, which proves that there is a strong coupling between them and also supports the conclusion in Fig. 3. At the same time, the strong MD mode can be found in the z-direction, which produces an ultra-narrow subradiant mode under mutual interference with the ED oscillation, resulting in the leakage of the energy, and behaves as a an extremely narrow linewidth Fano lineshape in the continuous spectrum. In addition, the multipolar decomposition results corresponding to $\alpha = 0$ show that its eigen Dipole resonance is dominated by ED (see Supplementary Material Fig. S6). For eigen Dipole mode, U-RCR and D-RCR excite a pair of co-directional current oscillations, and there is no obvious coupling between them. The corresponding MD mode is significantly weaker than that of QBIC state (Fig. 4b, left). And when in the symmetry-protected BIC state, U-RCR and DRCR each excites two pairs of reverse current oscillations respectively, which support the radiation-free EQ mode and correspond to the weak magnetic field distribution (Fig. 4b, middle).

### 3.4. Sensing performance analysis

In the above analysis of the sensing mechanism of QBIC resonance, we give the theoretical inference that QBIC resonance has stronger sensing ability than that of Dipole resonance. Here, we simulated a thin-layer analyte on the metasurface ($\alpha = 0.5$) and quantified the sensing performance of these two resonances by changing the refractive index (1.0 ~ 2.0 RIU) and thickness of the analyte (0 ~ 20 μm), where RIU is the refractive index unit. The refractive index range used here covers a series of important biological or chemical materials for THz sensing application. As shown in Fig. 5a & b, when the analyte thickness remains constant, as the refractive index increases, the frequency shift of Dipole resonance and QBIC resonance all increase linearly. Here, the frequency shift is calculated as $\Delta f = f(t) - f(t_0)$, where $f(t)$ is the resonant frequency when the analyte thickness is $t$ μm, and $f(t_0)$ is the resonant frequency when the analyte thickness is 0 μm (bare metasurface). We also introduce $S = \Delta f / \Delta n$ to describe the refractive index sensitivity of the biosensor, where $\Delta n$ is the unit change of the analyte refractive index, and calculated that $S_{QBIC} = 420$ GHz/RIU and $S_{Dipole} = 340$ GHz/RIU. Fig. 5c shows that for QBIC resonance, when the refractive index of the analyte is fixed at 2 RIU, with the analyte thickness increases from 0 to 5 μm, $\Delta f$ increases rapidly from 0 to 380 GHz. When the analyte thickness increases from 5 to 15 μm, $\Delta f$ grows slowly and eventually reaches saturation at 20 μm. The existence of the saturation region here is because that as the increase of the analyte thickness, the upper part of the analyte gradually approaches or even exceeds the edge of the bound light field. Correspondingly, its out-of-field part is difficult to interact with the electromagnetic energy constrained by the metasurface, which resulting in frequency shift saturation. For Dipole resonance, its $\Delta f$ is always significantly lower than that of QBIC resonance, and also reaches saturation at 20 μm. It is worth noting that for thin-layer analyte of 5 μm, the frequency shift of QBIC resonance ($\Delta f = 380$ GHz) increase by at least 100 GHz compared to that of Dipole resonance ($\Delta f = 280$ GHz), which means that the QBIC metasurface is more sensitive to ultrathin analyte. Therefore, these results further verify that QBIC resonance has a better sensing performance. In addition, the corresponding sensing results of when ultrathin analyte completely or partially covers the metasurface unit are also considered. The results show that the frequency shift provided by the effective sensing area of QBIC mode is equivalent to 76% of that of the entire metasurface unit, although the area of the former is about 10% of that of the latter (see Supplementary Material S6 for details).

### 3.5. Measurement and performance comparison of metasurface samples

We select the metasurface structure of $\alpha = 0.5$ for processing and measurement, because it has been proved to have the ideal comprehensive performance. The measured spectra in Fig. 6a show Dipole resonance at low frequency (1.753 THz) and QBIC resonance at high frequency (2.103 THz), respectively. Considering the limitation of instrument accuracy, we also refer to the structural parameters for simulation feedback. The comparison results show that the measured QBIC
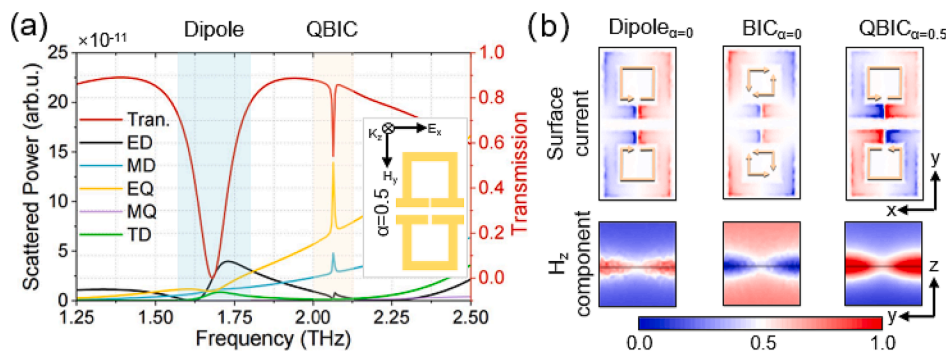


**Fig. 4.** Multipolar decomposition and mode distribution of the QBIC metasurface. (a) Multipolar decomposition result for the far-field scattering power of the metasurface at $\alpha = 0.5$. The inset gives the corresponding structure and polarization conditions. (b) The surface current distribution in the x-y plane and the z component of the magnetic field in the y-z plane corresponding to Dipole mode, BIC state and QBIC mode, respectively.
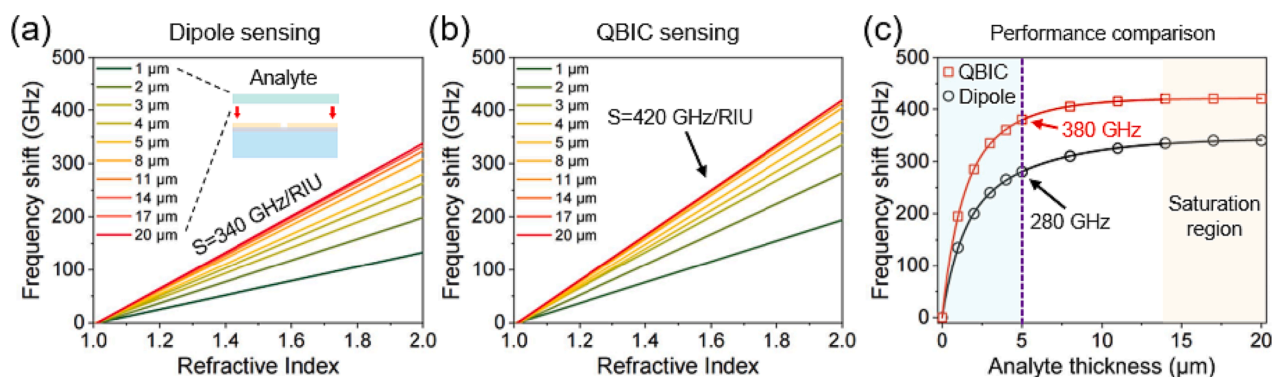
**Fig. 5.** Simulation of refractive index sensing of Dipole resonance and QBIC resonance. (a) For Dipole resonance, frequency shift law caused by analytes with different thickness and refractive index. (b) For QBIC resonance, frequency shift law caused by analytes with different thickness and refractive index. (c) Compared the sensing limits of Dipole resonance (black) and QBIC resonance (red), in which the refractive index is fixed to 2. Yellow shaded area is the saturation region for frequency shift. The nonlinear fit to the data points was performed, all with $R^2 > 0.99$. (For interpretation of the references to colour in this figure legend, the reader is referred to the web version of this article.)
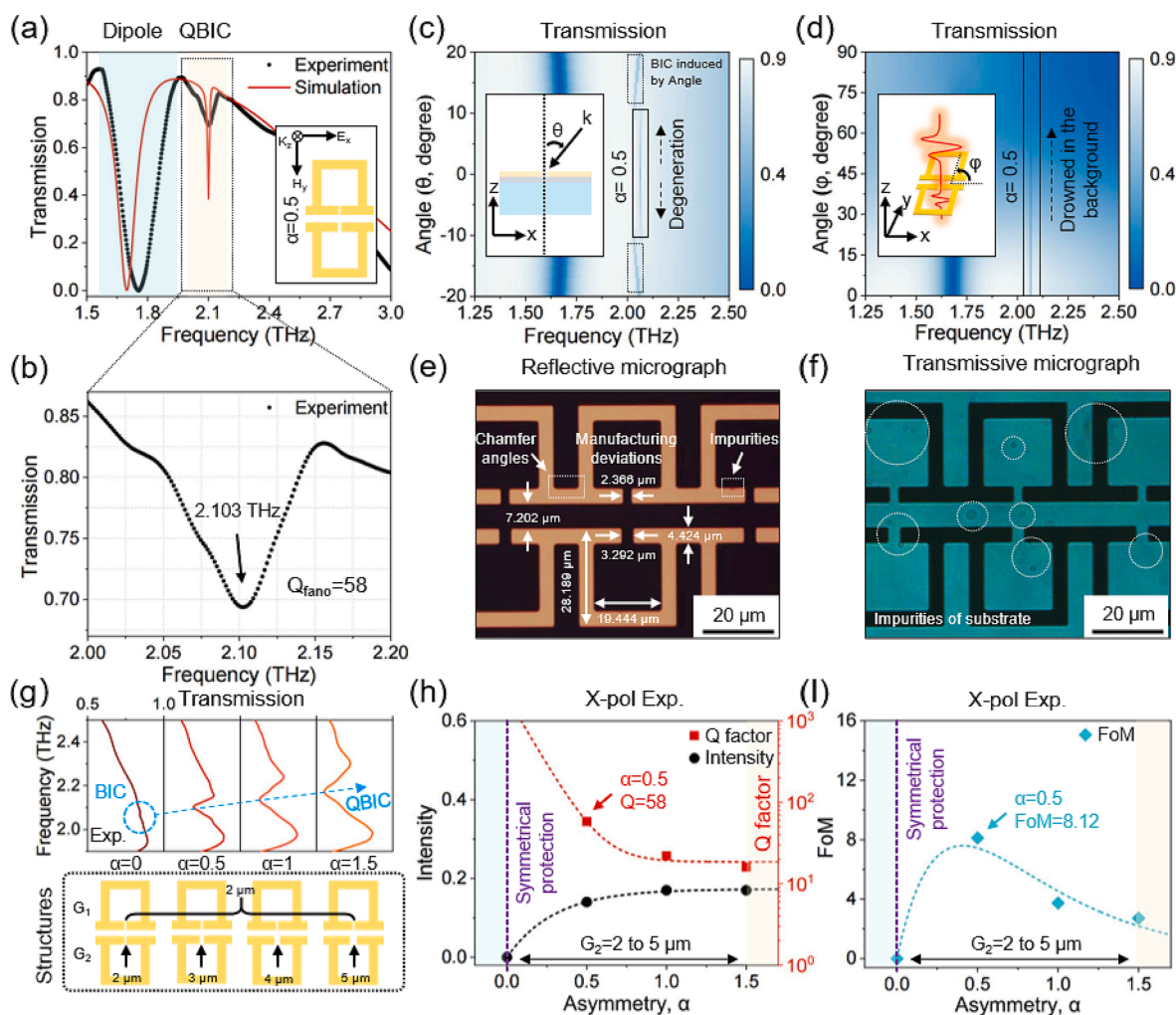


**Fig. 6.** The performance parameters of the fabricated QBIC metasurface biosensor ($\alpha = 0.5$). (a,b) Compared the measured (black) and simulated (red) results of the QBIC metasurface, and the position of QBIC is amplified. The inset gives the corresponding structure and polarization conditions. (c,d) Simulated the response of QBIC metasurface under non-vertical incident THz waves or different polarization angles incident THz waves. (e,f) Reflective and transmissive micrographs of QBIC metasurface. The actual machined dimensions of the key parameters are marked with white arrows and the machined chamfering and impurity defects are marked with dotted boxes or circles. (Scale bar = 20 μm). (g) The QBIC spectra and structural diagrams corresponding to QBIC metasurfaces ($\alpha = 0,0.5,1,1.5$). The BIC position is marked with a virtual coil, and the evolution of the QBIC lineshape is tracked with an arrow. (h,i) Extracted resonance intensity and Q factor of QBIC corresponding to different asymmetry $\alpha$, and calculated the FoM value. The nonlinear fit to the data points was performed, all with $R^2 > 0.99$. (For interpretation of the references to colour in this figure legend, the reader is referred to the web version of this article.)

resonance position is basically consistent with the simulation result, and the measured Dipole resonance has a slight blue shift. Here, the measured Q factor of QBIC resonance is 58 (Fig. 6b). It is well known that the experimental value of Q factor is usually lower than the simulated value, so this measurement result does not reach the optimal state. Our research suggests that there may be many factors that jointly cause the degeneration of Q factor: 1) Non-vertical incident terahertz waves will cause the intensity attenuation and broadening of QBIC resonance (Fig. 6c), and we also found the influence of additional BIC states excited by angular asymmetry; 2) The influence of polarization angle will make QBIC drowned in the background (Fig. 6d); 3) The manufacturing tolerance of micro-nano fabrication technology tends to show a Gaussian distribution, thus affecting the robustness of resonance (Fig. 6e); 4) Sample materials, rough surfaces and impurities will lead to inevitable Ohmic, scattering and impurity losses (Fig. 6f); 5) The resolution ratio limitation of the terahertz spectrometer used cannot observe the QBIC lineshape that should have been narrower. In Fig. 6g, we further fabricated the metasurface samples of α = 0, 0.5, 1 and 1.5, and the spectral measurement results clearly show the evolution trend of QBIC. In Fig. 6h, for the series of excited QBIC, although the Q factor and the resonance intensity have a certain degeneration, the variation trend is consistent with that of Fig. 2c & d, and the evolution of the Q factor still follows the inverse-square law $\alpha^{-2}$. The results in Fig. 6i further prove that the metasurface of α = 0.5 can be used as an ideal biosensing platform because it has the best FoM value. Therefore, we experimentally demonstrated the QBIC characteristics of the proposed metasurface.

In Table 1, we also listed the performance parameters of this work and that of the recently reported metasurface biosensors. We compared the Q factor and refractive index sensitivity of these metasurfaces, and pay more attention to whether they have been experimentally verified. It can be found that the maximum measured Q factor of the reported metasurface biosensor is 25, and the maximum refractive index sensitivity is 200 GHz/RIU, which are far lower than the index in our work. It should be noted that the THz metasurfaces in the table mainly excites resonance near or below 1 THz, and its larger resonator structure can weaken the influence of manufacturing tolerance. However, their performance may further degrade when scaled to high frequencies. The excellent performance of our fabricated metasurface at high frequency position also proves its high tolerance margin for manufacturing. The comparison results show that the QBIC metasurface biosensor in our work can realize high sensitivity sensing near 2 THz, and has the best comprehensive performance in Q factor and refractive index sensitivity.

### 3.6. Trace molecular sensing supported by QBIC metasurface

We use the proposed QBIC metasurface biosensor to challenge the detection of trace Hcy molecules to demonstrate its ability for clinical application. Hcy is the key biomarker molecule produced in the human body that reflects cardiovascular and cerebrovascular diseases, Alzheimer's disease, schizophrenia, inflammatory diseases, etc. The detection of Hcy concentration is of great significance for the diagnosis of these clinical diseases (for the introduction of Hcy, see Supplementary Material S1 for details). Here, we used the field emission scanning electron microscope (ZEISS Gemini SEM) to characterize the dried Hcy samples (Fig. 7a), and obtained the representative sample distribution image (Fig. 7b). It can be found that the dried Hcy molecules are randomly attached to the metasurface in the form of films, and the probability of the sample molecules falling in the B region (QBIC sensing range) is much larger than that in the A region (Dipole sensing range). Considering wide-area and intense light-matter interaction supported by QBIC resonance and the low-density distribution of trace samples, QBIC resonance is more likely to capture and detect the presence of trace molecules than Dipole. The sensing results of QBIC resonance and Dipole resonance in the THz band are given in Fig. 7c. It can be found that with the increase of the sample molecular concentration, the Dipole resonance and QBIC resonance occur red shift. In Fig. 7d, we intuitively compared the frequency shift between these two modes at different sample concentrations. Among them, QBIC resonance shows more significant frequency shift sensing performance when detecting samples at lower concentrations, and its direct Lod for Hcy is 12.5 pmol/μL, which is at least 40-times better than that of Dipole resonance (0.5 nmol/μL). Therefore, we have realized the pmol level detection of Hcy based on QBIC metasurface biosensor for the first time, and verified the excellent performance of the proposed metasurface in trace molecular sensing both theoretically and experimentally. It should be noted that the LoD obtained is constrained by the spectral resolution (7.6 GHz) of the instrument currently used, although the proposed metasurface may have potentially better performance. Of course, we also plan to develop and select materials with lower loss to improve the actual performance of the

**Table 1**
List for performance parameters of recently reported metasurfaces.

| Resonator material | Resonance type | Resonance position | Analyte | RI sensitivity | Q factor | Ref. |
|---|---|---|---|---|---|---|
| Gold | EIT-like resonance | 1.02 THz | Dielectric layer | 131.05 GHz/RIU | 10 (Sim.) 8.5 (Exp.) | [38] |
| Gold | LC resonance | 0.75 THz | Dielectric layer | 123.45 GHz/RIU | 100 (Sim.) 25 (Exp.) | [44] |
| Graphene | LSP resonance | 1.55 THz | Dielectric layer | 66 GHz/RIU | 32 (Sim.) None (Exp.) | [13] |
| Aluminium | Lattice-Enhanced Resonances-BIC | 0.96 THz | / | / | > 59 (Sim.) None (Exp.) | [14] |
| Gold | LSP resonance | 512.7 nm | Dielectric layer | 183 nm/RIU | None (Sim.) 10.3 (Exp.) | [25] |
| Aluminium | Guided mode resonance | 0.6 THz | Dielectric layer | 60 GHz/RIU | 10 (Sim.) 6 (Exp.) | [37] |
| Gold | TD resonance-BIC | 1.17 THz | Dielectric layer | 165 GHz/RIU | > 100 (Sim.) 16 (experiment) | [21] |
| Gold + Ge | Fano resonance-BIC | 0.66 THz | Dielectric layer | 24.5 GHz/RIU | > 75 (Sim.) 6.45 (Exp) | [62] |
| Stainless-steel | Anapole resonance | 0.26 THz | / | / | 14.5 (Sim.) 8.67 (Exp.) | [73] |
| Gold | Dipole resonance | 0.84 THz | Dielectric layer | 200 GHz/RIU | 2.1 (Sim.) 1.7 (Exp) | [74] |
| Graphene | Fano resonance | 0.39 THz | / | / | 6.83 (Sim.) 4.88 (Exp.) | [75] |
| Gold | Fano resonance-BIC | 2.065 THz | Dielectric layer | 420 GHz/RIU | ≥503 (Sim.) 58 (Exp.) | **This work** |
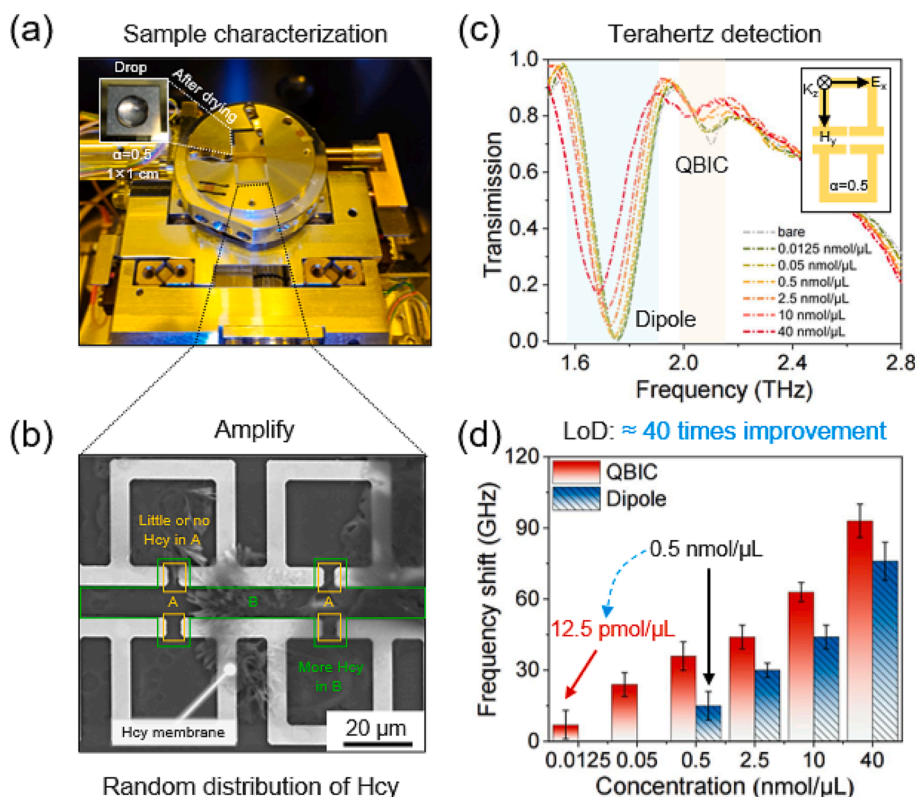
**Fig. 7.** Direct detection of trace molecules at pmol level based on QBIC metasurface of $\alpha = 0.5$. (a) SEM characterization of dried samples (Hcy) on the metasurface. The size of the cut chip is $1 \times 1$ cm.(b) The random distribution of Hcy molecular film on the metasurface. The A region (yellow) corresponds to Dipole sensing, and the B region (green) corresponds to QBIC sensing. (Scale bar = 20 μm).(c) The transmission spectrum changes of the metasurface caused by different concentrations of Hcy. The inset gives the corresponding structure and polarization conditions. (d) Extracted and compared the frequency shifts of QBIC resonance and Dipole resonance, and the direct LoD of QBIC resonance is 12.5 pmol/μL. (For interpretation of the references to colour in this figure legend, the reader is referred to the web version of this article.)

metasurface, and make it become a general platform for trace biochemical molecular sensing, and further explore the application of combining flexible substrates and microfluidic channels in clinical diagnosis. In addition, many biological and chemical reactions are usually accompanied by changes in the environment refractive index [76,77], and our proposed ultrasensitive biosensor can be used to monitor the entire process of these reactions. In the latest research, THz waves at specific frequencies could be used to induce hydrogen bond cleavage of DNA bases, thus establishing an efficient method for remotely driving in situ assembly of DNA origami [78]. Therefore, this work may have new and important applications in the fields of photocatalysis and photobiomodulation due to its efficient light field modulation ability. And related research work is currently under way and will be reported in the future.

## 4. Conclusion

In summary, we show a new QBIC metasurface and its sensing application. By manipulating the interference coupling between the electric quadrupole and the magnetic dipole, the ultrahigh quality QBIC resonance can be excited, and it will support wide-area and intense light-matter interaction. Specifically, by introducing asymmetry in the metasurface, we break the symmetry-protected BIC state and form an extremely narrow lineshape QBIC resonance. In this mode, the constrained electromagnetic energy and the effective sensing area will be greatly increased by about 400 % and 1300 %, respectively. The formed wide-area and ultra-strong photoactive region will greatly improve the capture probability of the biosensor for trace molecules and promote the coupling of the light field energy with the sample molecules. Simulated and experimental results show that the QBIC metasurface has an ultrahigh Q factor of 503 and a high sensitivity of 420 GHz/RIU, which can realize direct detection of trace molecules at pmol level. Its LoD also improves by at least 40 times than that of the classic Dipole mode. Compared with the reported references, this new QBIC metasurface has the best comprehensive performance. Its structure is simple and easy to

be fabricated, which is not only suitable for THz band, but can also be expanded and applied to the medium or near infrared bands through simple structural scaling. More exciting, the combination of advanced metasurface-nanoparticles system is expected to push the application of this new QBIC metasurface to a new height. Our work will be helpful to realize high precision sensing of trace biochemical molecules and promote the development and application of optical nonlinear platform with ultrahigh Q factor.

**CRediT authorship contribution statement**

**Bingwei Liu:** Investigation, Methodology, Software, Writing – original draft, Writing – review & editing. **Yan Peng:** Funding acquisition, Supervision, Writing – review & editing. **Zuanming Jin:** Funding acquisition, Supervision. **Xu Wu:** Investigation. **Hongyu Gu:** Investigation. **Dongshan Wei:** Funding acquisition, Supervision, Writing – review & editing. **Yiming Zhu:** Funding acquisition, Supervision. **Songlin Zhuang:** Funding acquisition, Supervision.

**Declaration of Competing Interest**

The authors declare that they have no known competing financial interests or personal relationships that could have appeared to influence the work reported in this paper.

**Data availability**

Data will be made available on request.

Key Domestic Scientific and Technological Cooperation Projects in Shanghai (21015800200).

## Appendix A. Supplementary data

Supplementary data to this article can be found online at https://doi.org/10.1016/j.cej.2023.142347.

## References

[1] N. Yu, P. Genevet, M.A. Kats, F. Aieta, J.P. Tetienne, F. Capasso, Z. Gaburro, Light propagation with phase discontinuities: generalized laws of reflection and refraction, Science 334 (6054) (2011) 333–337, https://doi.org/10.1126/science.1210713.

[2] H. Yao, X. Yan, M. Yang, Q. Yang, Y. Liu, A. Li, M. Wang, D. Wei, Z. Tian, L. Liang, Frequency-dependent ultrasensitive terahertz dynamic modulation at the Dirac point on graphene-based metal and all-dielectric metamaterials, Carbon 184 (2021) 400–408, https://doi.org/10.1016/j.carbon.2021.08.023.

[3] Y. Zhang, Y. Feng, J. Zhao, Graphene-enabled tunable multifunctional metamaterial for dynamical polarization manipulation of broadband terahertz wave, Carbon 163 (2020) 244–252, https://doi.org/10.1016/j.carbon.2020.03.001.

[4] S. Sun, Q. He, J. Hao, S. Xiao, L. Zhou, Electromagnetic metasurfaces: physics and applications, Adv. Opt. Photon. 11 (2) (2019) 380, https://doi.org/10.1364/aop.11.000380.

[5] Z.-L. Deng, T. Fu, Z. Ouyang, G.P. Wang, Trimeric metasurfaces for independent control of bright and dark modes of Fano resonances, Appl. Phys. Lett. 108 (8) (2016) 081109, https://doi.org/10.1063/1.4942644.

[6] G. Zheng, H. Muhlenbernd, M. Kenney, G. Li, T. Zentgraf, S. Zhang, Metasurface holograms reaching 80% efficiency, Nat. Nanotechnol. 10 (4) (2015) 308–312, https://doi.org/10.1038/nnano.2015.2.

[7] S. Colburn, A. Zhan, A. Majumdar, Metasurface optics for full-color computational imaging, Sci. Adv. 4 (2) (2018), https://doi.org/10.1126/sciadv.aar2114.

[8] Y. Zhang, S. Qiao, S. Liang, Z. Wu, Z. Yang, Z. Feng, H. Sun, Y. Zhou, L. Sun, Z. Chen, X. Zou, B. Zhang, J. Hu, S. Li, Q. Chen, L. Li, G. Xu, Y. Zhao, S. Liu, Gbps terahertz external modulator based on a composite metamaterial with a double-channel heterostructure, Nano Lett. 15 (5) (2015) 3501–3506, https://doi.org/10.1021/acs.nanolett.5b00869.

[9] S. Romano, M. Mangini, E. Penzo, S. Cabrini, A.C. De Luca, I. Rendina, V. Mocella, G. Zito, Ultrasensitive surface refractive index imaging based on quasi-bound states in the continuum, ACS Nano 14 (11) (2020) 15417–15427, https://doi.org/10.1021/acsnano.0c06050.

[10] X. Wu, B. Quan, X. Pan, X. Xu, X. Lu, C. Gu, L. Wang, Alkanethiol-functionalized terahertz metamaterial as label-free, highly-sensitive and specific biosensor, Biosens. Bioelectron. 42 (2013) 626–631, https://doi.org/10.1016/j.bios.2012.10.095.

[11] A. Danilov, G. Tselikov, F. Wu, V.G. Kravets, I. Ozerov, F. Bedu, A.N. Grigorenko, A.V. Kabashin, Ultra-narrow surface lattice resonances in plasmonic metamaterial arrays for biosensing applications, Biosens. Bioelectron. 104 (2018) 102–112, https://doi.org/10.1016/j.bios.2017.12.001.

[12] S.A. Khan, N.Z. Khan, Y. Xie, M.T. Abbas, M. Rauf, I. Mehmood, M. Runowski, S. Agathopoulos, J. Zhu, Optical sensing by metamaterials and metasurfaces: from physics to biomolecule detection, Adv. Opt. Mater. 10 (18) (2022) 2200500, https://doi.org/10.1002/adom.202200500.

[13] M.S. Islam, J. Sultana, M. Biabanifard, Z. Vafapour, M.J. Nine, A. Dinovitser, C.M. B. Cordeiro, B.W.H. Ng, D. Abbott, Tunable localized surface plasmon graphene metasurface for multiband superabsorption and terahertz sensing, Carbon 158 (2020) 559–567, https://doi.org/10.1016/j.carbon.2019.11.026.

[14] T.C.W. Tan, E. Plum, R. Singh, Lattice-enhanced fano resonances from bound states in the continuum metasurfaces, Adv. Opt. Mater. 8 (6) (2020) 1901572.

[15] S.R.K. Rodriguez, A. Abass, B. Maes, O.T.A. Janssen, G. Vecchi, J. Gómez Rivas, Coupling bright and dark plasmonic lattice resonances, Phys. Rev. X 1 (2) (2011), https://doi.org/10.1103/PhysRevX.1.021019.

[16] S. Baur, S. Sanders, A. Manjavacas, Hybridization of lattice resonances, ACS Nano 12 (2) (2018) 1618–1629, https://doi.org/10.1021/acsnano.7b08206.

[17] J. Gu, R. Singh, X. Liu, X. Zhang, Y. Ma, S. Zhang, S.A. Maier, Z. Tian, A.K. Azad, H.-T. Chen, A.J. Taylor, J. Han, W. Zhang, Active control of electromagnetically induced transparency analogue in terahertz metamaterials, Nat. Commun. 3 (1) (2012), https://doi.org/10.1038/ncomms2153.

[18] M. Chen, Z. Xiao, X. Lu, F. Lv, Y. Zhou, Simulation of dynamically tunable and switchable electromagnetically induced transparency analogue based on metal-graphene hybrid metamaterial, Carbon 159 (2020) 273–282, https://doi.org/10.1016/j.carbon.2019.12.050.

[19] P. Fan, Z. Yu, S. Fan, M.L. Brongersma, Optical Fano resonance of an individual semiconductor nanostructure, Nat. Mater. 13 (5) (2014) 471–475, https://doi.org/10.1038/nmat3927.

[20] M.F. Limonov, M.V. Rybin, A.N. Poddubny, Y.S. Kivshar, Fano resonances in photonics, Nat. Photonics 11 (9) (2017) 543–554, https://doi.org/10.1038/nphoton.2017.142.

[21] R. Wang, L. Xu, J. Wang, L. Sun, Y. Jiao, Y. Meng, S. Chen, C. Chang, C. Fan, Electric Fano resonance-based terahertz metasensors, Nanoscale 13 (44) (2021) 18467–18472, https://doi.org/10.1039/d1nr04477j.

[22] Y. Wu, L. Kang, H. Bao, D.H. Werner, Exploiting topological properties of mie-resonance-based hybrid metasurfaces for ultrafast switching of light polarization, ACS Photonics 7 (9) (2020) 2362–2373, https://doi.org/10.1021/acsphotonics.0c00858.

[23] S. Park, J. Cho, D. Jeong, J. Jo, M. Nam, H. Rhee, J.S. Han, Y.J. Cho, B.-K. Ju, D.-H. Ko, H.S. Jang, Simultaneous enhancement of luminescence and stability of CsPbBr 3 perovskite nanocrystals via formation of perhydropolysilazane-derived nanopatterned film, Chem. Eng. J. 393 (2020) 124767.

[24] J.C. Deinert, D. Alcaraz Iranzo, R. Perez, X. Jia, H.A. Hafez, I. Ilyakov, N. Awari, M. Chen, M. Bawatna, A.N. Ponomaryov, S. Germanskiy, M. Bonn, F.H.L. Koppens, D. Turchinovich, M. Gensch, S. Kovalev, K.J. Tielrooij, Grating-graphene metamaterial as a platform for terahertz nonlinear photonics, ACS Nano 15 (1) (2021) 1145–1154, https://doi.org/10.1021/acsnano.0c08106.

[25] R. Funari, K.Y. Chu, A.Q. Shen, Detection of antibodies against SARS-CoV-2 spike protein by gold nanospikes in an opto-microfluidic chip, Biosens Bioelectron 169 (2020), 112578, https://doi.org/10.1016/j.bios.2020.112578.

[26] Y. Hu, M. Tong, Z. Xu, X. Cheng, T. Jiang, Spatiotemporal terahertz metasurfaces for ultrafast all-optical switching with electric-triggered bistability, Laser Photonics Rev. 15 (3) (2021) 2000456, https://doi.org/10.1002/lpor.202000456.

[27] M. Manjappa, P. Pitchappa, N. Singh, N. Wang, N.I. Zheludev, C. Lee, R. Singh, Reconfigurable MEMS Fano metasurfaces with multiple-input-output states for logic operations at terahertz frequencies, Nat. Commun. 9 (1) (2018) 4056, https://doi.org/10.1038/s41467-018-06360-5.

[28] Y. Wang, B. Dai, C. Ma, Q. Zhang, K. Huang, X. Luo, X. Liu, Y. Ying, L. Xie, Cross-wavelength hierarchical metamaterials enabled for trans-scale molecules detection simultaneously, Adv. Sci. (Weinh) 9 (13) (2022) e2105447.

[29] D. Suzuki, S. Oda, Y. Kawano, A flexible and wearable terahertz scanner, Nat. Photonics 10 (12) (2016) 809–813, https://doi.org/10.1038/nphoton.2016.209.

[30] Y. Peng, C. Shi, Y. Zhu, M. Gu, S. Zhuang, Terahertz spectroscopy in biomedical field: a review on signal-to-noise ratio improvement, PhotoniX 1 (1) (2020), https://doi.org/10.1186/s43074-020-00011-z.

[31] Y. Peng, J. Huang, J. Luo, Z. Yang, L. Wang, X. Wu, X. Zang, C. Yu, M. Gu, Q. Hu, X. Zhang, Y. Zhu, S. Zhuang, Three-step one-way model in terahertz biomedical detection, PhotoniX 2 (1) (2021), https://doi.org/10.1186/s43074-021-00034-0.

[32] X. Wu, Y. E, X. Xu, L. Wang, Label-free monitoring of interaction between DNA and oxaliplatin in aqueous solution by terahertz spectroscopy, Appl. Phys. Lett. 101 (3) (2012) 033704.

[33] X. Yang, X. Zhao, K. Yang, Y. Liu, Y. Liu, W. Fu, Y. Luo, Biomedical applications of terahertz spectroscopy and imaging, Trends Biotechnol. 34 (10) (2016) 810–824, https://doi.org/10.1016/j.tibtech.2016.04.008.

[34] H. Yan, W. Fan, X. Chen, L. Liu, H. Wang, X. Jiang, Terahertz signatures and quantitative analysis of glucose anhydrate and monohydrate mixture, Spectrochim. Acta A Mol. Biomol. Spectrosc. 258 (2021), 119825, https://doi.org/10.1016/j.saa.2021.119825.

[35] Y. Peng, C. Shi, M. Xu, T. Kou, X. Wu, B. Song, H. Ma, S. Guo, L. Liu, Y. Zhu, Qualitative and quantitative identification of components in mixture by terahertz spectroscopy, IEEE Trans. Terahertz Sci. Technol. 8 (6) (2018) 696–701, https://doi.org/10.1109/tthz.2018.2867816.

[36] S.J. Park, J.T. Hong, S.J. Choi, H.S. Kim, W.K. Park, S.T. Han, J.Y. Park, S. Lee, D. S. Kim, Y.H. Ahn, Detection of microorganisms using terahertz metamaterials, Sci. Rep. 4 (2014) 4988, https://doi.org/10.1038/srep04988.

[37] M. Gupta, R. Singh, Terahertz sensing with optimized Q/Veff Metasurface cavities, Adv. Opt. Mater. 8 (16) (2020), https://doi.org/10.1002/adom.201902025.

[38] Z. Zhang, M. Yang, X. Yan, X. Guo, J. Li, Y. Yang, D. Wei, L. Liu, J. Xie, Y. Liu, L. Liang, J. Yao, The antibody-free recognition of cancer cells using plasmonic biosensor platforms with the anisotropic resonant metasurfaces, ACS Appl. Mater. Interfaces 12 (10) (2020) 11388–11396, https://doi.org/10.1021/acsami.0c00095.

[39] Z. Bai, Y. Liu, R. Kong, T. Nie, Y. Sun, H. Li, T. Sun, C. Pandey, Y. Wang, H. Zhang, Q. Song, G. Liu, M. Kraft, W. Zhao, X. Wu, L. Wen, Near-field terahertz sensing of hela cells and pseudomonas based on monolithic integrated metamaterials with a spintronic terahertz emitter, ACS Appl. Mater. Interfaces 12 (32) (2020) 35895–35902, https://doi.org/10.1021/acsami.0c08543.

[40] S.H. Lee, Y.K. Lee, S.H. Lee, J. Kwak, H.S. Song, M. Seo, Detection and discrimination of SARS-CoV-2 spike protein-derived peptides using THz metamaterials, Biosens. Bioelectron. 202 (2022) 113981, https://doi.org/10.1016/j.bios.2022.113981.

[41] R. Sengupta, H. Khand, G. Sarusi, Terahertz impedance spectroscopy of biological nanoparticles by a resonant metamaterial chip for breathalyzer-based COVID-19 prompt tests, ACS Appl. Nano Mater. 5 (4) (2022) 5803–5812, https://doi.org/10.1021/acsanm.2c00954.

[42] S.W. Jun, Y.H. Ahn, Terahertz thermal curve analysis for label-free identification of pathogens, Nat. Commun. 13 (1) (2022) 3470, https://doi.org/10.1038/s41467-022-31137-2.

[43] W. Shi, F. Fan, S. Li, Z. Zhang, H. Liu, X. Wang, S. Chang, Terahertz immunosensing assisted by functionalized Au NPs based on all-dielectric metasurface, Sens. Actuators B 362 (2022) 131777.

[44] K. Yang, J. Li, M. Lamy de la Chapelle, G. Huang, Y. Wang, J. Zhang, D. Xu, J. Yao, X. Yang, W. Fu, A terahertz metamaterial biosensor for sensitive detection of microRNAs based on gold-nanoparticles and strand displacement amplification, Biosens. Bioelectron. 175 (2021), 112874, https://doi.org/10.1016/j.bios.2020.112874.

[45] L. Wang, X. Wu, X. Peng, Q. Yang, X. Chen, W. Wu, Y. Zhu, S. Zhuang, Quantitative analysis of homocysteine in liquid by terahertz spectroscopy, Biomed. Opt. Express 11 (5) (2020) 2570–2577, https://doi.org/10.1364/BOE.391894.

[46] C.W. Hsu, B. Zhen, A.D. Stone, J.D. Joannopoulos, M. Soljačić, Bound states in the continuum, Nat. Rev. Mater. 1 (9) (2016), https://doi.org/10.1038/natrevmats.2016.48.

[47] S. Joseph, S. Pandey, S. Sarkar, J. Joseph, Bound states in the continuum in resonant nanostructures: an overview of engineered materials for tailored applications, Nanophotonics 10 (17) (2021) 4175–4207, https://doi.org/10.1515/nanoph-2021-0387.

[48] C.W. Qiu, T. Zhang, G. Hu, Y. Kivshar, Quo Vadis, Metasurfaces? Nano Lett. 21 (13) (2021) 5461–5474, https://doi.org/10.1021/acs.nanolett.1c00828.

[49] S. Yang, C. Hong, Y. Jiang, J.C. Ndukaife, Nanoparticle trapping in a Quasi-BIC system, ACS Photonics 8 (7) (2021) 1961–1971, https://doi.org/10.1021/acsphotonics.0c01941.

[50] S. Han, P. Pitchappa, W. Wang, Y.K. Srivastava, M.V. Rybin, R. Singh, Extended bound states in the continuum with symmetry-broken terahertz dielectric metasurfaces, Adv. Opt. Mater. 9 (7) (2021) 2002001.

[51] L. Cong, R. Singh, Symmetry-protected dual bound states in the continuum in metamaterials, Adv. Opt. Mater. (2019), https://doi.org/10.1002/adom.201900383.

[52] C.W. Hsu, B. Zhen, J. Lee, S.-L. Chua, S.G. Johnson, J.D. Joannopoulos, M. Soljačić, Observation of trapped light within the radiation continuum, Nature 499 (7457) (2013) 188–191, https://doi.org/10.1038/nature12289.

[53] Y.K. Srivastava, R.T. Ako, M. Gupta, M. Bhaskaran, S. Sriram, R. Singh, Terahertz sensing of 7 nm dielectric film with bound states in the continuum metasurfaces, Appl. Phys. Lett. 115 (15) (2019) 151105, https://doi.org/10.1063/1.5110383.

[54] J. Li, J. Li, C. Zheng, Z. Yue, S. Wang, M. Li, H. Zhao, Y. Zhang, J. Yao, Free switch between bound states in the continuum (BIC) and quasi-BIC supported by graphene-metal terahertz metasurfaces, Carbon 182 (2021) 506–515, https://doi.org/10.1016/j.carbon.2021.06.037.

[55] H.M. Doeleman, F. Monticone, W. den Hollander, A. Alù, A.F. Koenderink, Experimental observation of a polarization vortex at an optical bound state in the continuum, Nat. Photonics 12 (7) (2018) 397–401, https://doi.org/10.1038/s41566-018-0177-5.

[56] T. Dong, S. Li, M. Manjappa, P. Yang, J. Zhou, D. Kong, B. Quan, X. Chen, C. Ouyang, F. Dai, J. Han, C. Ouyang, X. Zhang, J. Li, Y. Li, J. Miao, Y. Li, L. Wang, R. Singh, W. Zhang, X. Wu, Nonlinear THz-Nano Metasurfaces, Adv. Funct. Mater. 31 (24) (2021) 2100463.

[57] A. Kodigala, T. Lepetit, Q. Gu, B. Bahari, Y. Fainman, B. Kante, Lasing action from photonic bound states in continuum, Nature 541 (7636) (2017) 196–199, https://doi.org/10.1038/nature20799.

[58] A. Tittl, A. Leitis, M. Liu, F. Yesilkoy, D.-Y. Choi, D.N. Neshev, Y.S. Kivshar, H. Altug, Imaging-based molecular barcoding with pixelated dielectric metasurfaces, Science 360 (6393) (2018) 1105–1109, https://doi.org/10.1126/science.aas9768.

[59] A. Leitis, A. Tittl, M. Liu, B.H. Lee, M.B. Gu, Y.S. Kivshar, H. Altug, Angle-multiplexed all-dielectric metasurfaces for broadband molecular fingerprint retrieval, Sci. Adv. 5 (5) (2019), https://doi.org/10.1126/sciadv.aaw2871.

[60] S. Romano, G. Zito, S. Torino, G. Calafiore, E. Penzo, G. Coppola, S. Cabrini, I. Rendina, V. Mocella, Label-free sensing of ultralow-weight molecules with all-dielectric metasurfaces supporting bound states in the continuum, Photonics Res. 6 (7) (2018) 726, https://doi.org/10.1364/prj.6.000726.

[61] Y. Chen, C. Zhao, Y. Zhang, C.W. Qiu, Integrated molar chiral sensing based on high-Q metasurface, Nano Lett. 20 (12) (2020) 8696–8703, https://doi.org/10.1021/acs.nanolett.0c03506.

[62] T.C. Tan, Y.K. Srivastava, R.T. Ako, W. Wang, M. Bhaskaran, S. Sriram, I. Al-Naib, E. Plum, R. Singh, Active control of nanodielectric-induced THz Quasi-BIC in flexible metasurfaces: a platform for modulation and sensing, Adv. Mater. 33 (27) (2021) e2100836, https://doi.org/10.1002/adma.202100836.

[63] A.S. Lal Krishna, S. Menon, A. Prosad, V. Raghunathan, Mid-infrared quasi-BIC resonances with sub-wavelength slot mode profiles in germanium-based coupled guided-mode resonance structures, Photonics Res. 10 (1) (2021), https://doi.org/10.1364/prj.442650.

[64] S. Yang, M. He, C. Hong, J.D. Caldwell, J.C. Ndukaife, Engineering electromagnetic field distribution and resonance quality factor using slotted Quasi-BIC metasurfaces, Nano Lett 22 (20) (2022) 8060–8067, https://doi.org/10.1021/acs.nanolett.2c01919.

[65] X. Du, L. Xiong, X. Zhao, S. Chen, J. Shi, G. Li, Dual-band bound states in the continuum based on hybridization of surface lattice resonances, Nanophotonics 11 (21) (2022) 4843–4853, https://doi.org/10.1515/nanoph-2022-0427.

[66] J. Kühne, J. Wang, T. Weber, L. Kühner, S.A. Maier, A. Tittl, Fabrication robustness in BIC metasurfaces, Nanophotonics 10 (17) (2021) 4305–4312, https://doi.org/10.1515/nanoph-2021-0391.

[67] S.I. Azzam, A.V. Kildishev, Photonic bound states in the continuum: from basics to applications, Adv. Opt. Mater. 9 (1) (2021) 2001469, https://doi.org/10.1002/adom.202001469.

[68] A. Ndao, L. Hsu, W. Cai, J. Ha, J. Park, R. Contractor, Y. Lo, B. Kanté, Differentiating and quantifying exosome secretion from a single cell using quasi-bound states in the continuum, Nanophotonics 9 (5) (2020) 1081–1086, https://doi.org/10.1515/nanoph-2020-0008.

[69] X. Zhao, C. Chen, K. Kaj, I. Hammock, Y. Huang, R.D. Averitt, X. Zhang, Terahertz investigation of bound states in the continuum of metallic metasurfaces, Optica 7 (11) (2020) 1548, https://doi.org/10.1364/optica.404754.

[70] C. Kyaw, R. Yahiaoui, J.A. Burrow, V. Tran, K. Keelen, W. Sims, E.C. Red, W. S. Rockward, M.A. Thomas, A. Sarangan, I. Agha, T.A. Searles, Polarization-selective modulation of supercavity resonances originating from bound states in the continuum, Commun. Phys. 3 (1) (2020), https://doi.org/10.1038/s42005-020-00453-8.

[71] K. Koshelev, S. Lepeshov, M. Liu, A. Bogdanov, Y. Kivshar, Asymmetric metasurfaces with high-Q Resonances governed by bound states in the continuum, Phys. Rev. Lett. 121 (19) (2018), 193903, https://doi.org/10.1103/PhysRevLett.121.193903.

[72] S. Li, C. Zhou, T. Liu, S. Xiao, Symmetry-protected bound states in the continuum supported by all-dielectric metasurfaces, Phys. Rev. A 100 (6) (2019), https://doi.org/10.1103/PhysRevA.100.063803.

[73] X. Li, J. Yin, J. Liu, F. Shu, T. Lang, X. Jing, Z. Hong, Resonant transparency of a planar anapole metamaterial at terahertz frequencies, Photonics Res. 9 (2) (2021) 125, https://doi.org/10.1364/prj.413361.

[74] C. Tang, J. Yang, Y. Wang, J. Cheng, X. Li, C. Chang, J. Hu, J. Lü, Integrating terahertz metamaterial and water nanodroplets for ultrasensitive detection of amyloid β aggregates in liquids, Sens. Actuators B 329 (2021) 129113, https://doi.org/10.1016/j.snb.2020.129113.

[75] R. Zhou, C. Wang, Y. Huang, K. Huang, Y. Wang, W. Xu, L. Xie, Y. Ying, Label-free terahertz microfluidic biosensor for sensitive DNA detection using graphene-metasurface hybrid structures, Biosens. Bioelectron. 188 (2021) 113336, https://doi.org/10.1016/j.bios.2021.113336.

[76] J. Zhou, X. Zhao, G. Huang, X. Yang, Y. Zhang, X. Zhan, H. Tian, Y. Xiong, Y. Wang, W. Fu, Molecule-specific terahertz biosensors based on an aptamer hydrogel-functionalized metamaterial for sensitive assays in aqueous environments, ACS Sens. 6 (5) (2021) 1884–1890, https://doi.org/10.1021/acssensors.1c00174.

[77] J. Gao, Y. Li, J. Liu, D. Ling, X. Deng, B. Liu, R. Li, D. Wei, Terahertz spectroscopy detection of lithium citrate tetrahydrate and its dehydration kinetics, Spectrochim. Acta A Mol. Biomol. Spectrosc. 266 (2022), 120470, https://doi.org/10.1016/j.saa.2021.120470.

[78] C. Zhang, Y. Yuan, K. Wu, Y. Wang, S. Zhu, J. Shi, L. Wang, Q. Li, X. Zuo, C. Fan, C. Chang, J. Li, Driving DNA origami assembly with a terahertz wave, Nano Lett. 22 (1) (2022) 468–475, https://doi.org/10.1021/acs.nanolett.1c04369.